Check for updates

Small

NANO · MICRO small
www.small-journal.com

RESEARCH ARTICLE

Mechanically Driven, Self-Powered Hydrogel Iontronics for Visualized Tactile Logic Gate Circuit

Yaowen Ouyang[1,2] | Xing Xiang[3] | Yuyang Zhang[1] | Xiang Li[1] | Yanguang Zhou[3] | Zhong Lin Wang[1] | Di Wei[1,4]

[1]Beijing Institute of Nanoenergy and Nanosystems, Chinese Academy of Sciences, Beijing, P. R. China | [2]School of Nanoscience and Engineering, University of Chinese Academy of Sciences, Beijing, P. R. China | [3]Department of Mechanical and Aerospace Engineering, the Hong Kong University of Science and Technology, Kowloon, Hong Kong SAR, P. R. China | [4]Centre For Photonic Devices and Sensors, University of Cambridge, Cambridge, UK

Correspondence: Yanguang Zhou (maeygzhou@ust.hk) | Di Wei (weidi@binn.cas.cn)

Received: 3 February 2026 | **Revised:** 14 April 2026 | **Accepted:** 4 May 2026

Keywords: hydrogel iontronics | ion transport behavior modulation | piezoionic nanogenerator | self-powered device | visualized tactile logic gate circuit

ABSTRACT

The modulation of ion transport underlies neuronal signal integration, yet achieving self-powered tactile logic based on ionic mechanisms remains challenging. Here we report a hydrogel iontronic platform that mimics neuronal threshold-triggered action potentials and enables mechano-driven, self-powered logic processing. A polyvinyl alcohol/polyacrylamide (PVA/PAM) double-network hydrogel with engineered geometric, mechanical, and impedance asymmetry exhibits pronounced nonlinear ion gating, delivering peak ionic current densities of ~2 mA cm^{-2} at 72.68 kPa (0.275 A m^{-2} kPa^{-1}), exceeding state-of-the-art devices and orders of magnitude higher than conventional piezoionic systems. Molecular dynamics simulations reveal that interactions between NO_3^- and water molecules in hydrogel invert diffusion asymmetry, providing deterministic control over ionic transport. Electrolyte selection enables programmable switching between excitatory and inhibitory ionic outputs, allowing realization of four fundamental self-powered Boolean logic gates (OR, AND, NOR, and NAND) through simple series-parallel integration. Coupling triboelectric nanogenerators (TENG) enables real-time visualized tactile logic via LED outputs. This work advances hydrogel iontronics from passive sensing toward integrated perception-cognition, opening new routes for neuromimetic human-machine interfaces (HMI) and Internet-of-Things (IoT) systems.

1 | Introduction

Ion transport is a fundamental process that unifies physics, chemistry, and life, governing how living systems sense, compute, and respond to their environment in ways fundamentally distinct from electronic devices [1–3]. From the generation and propagation of action potentials in neurons to energy storage in batteries and molecular exchange across biological membranes, many essential biological and technological processes rely on the precise, directional movement of ions through confined media and selective pathways [4–6]. As a consequence, the regulation of ion transport is not only a central problem in basic science, but also a key driver of innovation in energy technologies, bioelectronics, environmental sensing and information processing [7, 8]. In this context, iontronics refers to a class of devices that use ions as the primary charge carriers, rather than electrons, establishing an information and energy transduction paradigm that is fundamentally distinct from conventional electronics based on electronic conduction [9–12]. Despite remarkable advances in electronics-based artificial intelligence, a profound physical mismatch

Yaowen Ouyang, and Xing Xiang contributed equally to this work.

© 2026 Wiley-VCH GmbH

remains between electronic and biological computation [13, 14]. Modern computers achieve extraordinary processing speed, yet at the cost of orders-of-magnitude higher power consumption than the human brain, which operates at ~20 W with minimal heat dissipation [15]. This gap arises from a fundamental difference in carrier physics: electrons dominate in solid-state devices, whereas ions govern information transmission in biological systems. In the nervous system, neural signaling, synaptic plasticity, and memory formation all emerge from transmembrane ion transport and the spatiotemporal modulation of ionic fluxes [16]. Neuromorphic systems aim to emulate these principles beyond the von-Neumann architecture, yet existing silicon-based electronic transistors and memristors remain constrained by rigid materials, centralized power supply, Joule heating and electromagnetic interference [17–20]. By contrast, ionic systems offer intrinsic biocompatibility, low-energy operation and noise immunity, positioning ion-based information processing as a promising route toward physically embodied intelligence. Existing flexible neuromorphic devices have made great progress, significantly reducing power consumption in functions such as sensing and computing [19]. However, these devices are mostly controlled by an applied voltage, while the inherent energy properties of ions have been largely overlooked. The development of self-powered neuromorphic systems represents a promising direction.

Hydrogels, comprising three-dimensional polymer networks swollen with water, provide a particularly compelling platform for such ion-based systems [21]. Their softness, high water content, and mechanical compliance closely match those of biological tissues, while their polymer architectures define ion pathways, selectivity, and transport kinetics [22]. These features have enabled the emergence of piezoionic hydrogel devices, in which mechanical deformation induces transient separation of anions and cations by solvent convection, generating measurable voltages and currents without external bias [23]. Remarkably, piezoionic devices can reach charge densities several orders of magnitude higher than those of conventional piezoelectric or triboelectric generators [24], making them highly attractive for artificial skin, neural interfaces and wearable bioelectronics [25, 26]. Recent efforts to enhance piezoionic performance have focused on polymer network design [27, 28], electrode or electrolyte optimization [29–31], phase-interface engineering [32, 33] and structural gradients [34, 35], all aimed at amplifying the diffusion asymmetry between cations and anions [36]. Moreover, by exploiting ion size, charge, hydration and ion–polymer interactions, piezoionic systems have achieved tunable signal amplitudes, directions and relaxation dynamics.

Yet, signal generation alone does not constitute information processing. In biological neural networks, perception is inseparable from in situ computation: sensory inputs are threshold-filtered, weighted, integrated and converted into logical decisions directly at the synaptic level [37–39]. Although piezoionic hydrogels excel at self-powered sensing, the realization of integrated perception-cognition systems, where tactile signals are directly converted into logical operations without external circuitry, remains largely unexplored. Achieving such ion-based, in situ logical processing represents a critical frontier in hydrogel iontronics and neuromorphic engineering. Here we report a hydrogel-based iontronic platform that reproduces the threshold-triggered behavior of neuronal action potentials and enables fully self-powered tactile logic processing. Using a polyvinyl alcohol/polyacrylamide (PVA/PAM) double-network hydrogel and introducing asymmetric geometry, compositional modulus gradients, and impedance discontinuities, the device exhibits synaptic-like ion-gating behavior. With increasing compressive strain, the ionic current exhibits a pronounced nonlinear increase, reaching ~2 mA cm^{-2} at 72.68 kPa (0.275 A m^{-2} kPa^{-1}), representing an orders-of-magnitude enhancement over conventional piezoionic devices (Table S1), thereby mimicking subthreshold responses and action-potential firing. These two regimes naturally map onto binary logic states '0' and '1', enabling mechanical stimuli to be directly converted into recognizable digital information (Figure 1a).

Combined experiments and molecular dynamics simulations reveal that this nonlinear gating originates from Hofmeister-type interactions between chaotropic anions (NO_3^-) and PVA chains, which modulate cation hydration and invert the relative diffusion coefficients of anions and cations. This ion-polymer coupling provides a molecular mechanism for deterministic control of ion transport and electrical signal generation. By assembling hydrogel units that generate excitatory and inhibitory ionic outputs, we emulate synaptic weighting in neural networks. Simple series-parallel interconnections yield four fundamental self-powered logic gates (OR, AND, NOR, and NAND) driven purely by mechanical stimuli. To render these abstract ionic logic operations visually interpretable, we further integrate the hydrogel iontronics with triboelectric nanogenerators (TENG) that translate ionic current amplitudes into color-coded LED outputs, enabling real-time visualization of logical states and signal pathways (Figure 1b). Unlike conventional semiconductor logic, this system combines soft mechanics, ion-based charge carriers and autonomous energy generation, eliminating the need for external power sources while offering intrinsic biocompatibility and electromagnetic immunity. Together, this work establishes a self-powered, mechanically driven iontronic logic architecture in which sensing, memory and computation emerge directly from regulated ion transport in soft matter. By embedding Boolean logic at the source of tactile signal generation, it advances hydrogel-based iontronics from perception toward integrated cognition, opening new routes for neuromorphic systems, human–machine interfaces, distributed intelligence and next-generation Internet of Things architectures.

2 | Results and Disscussion

2.1 | Hydrogel Iontronics with Biomimetic Gating Behavior

In the biological nervous system, mechanical transduction occurs through the activation of ion channels, leading to the generation of receptor potentials [40]. When this potential exceeds a certain threshold, it triggers an action potential; when it remains below the threshold, a subthreshold response is produced [41]. By simulating the nonlinear activation behavior of biological neurons, it is possible to harness the potential of bionic information processing [42]. This principle underscores the bionic significance of achieving nonlinear electrical signal response in piezoionic hydrogels [43–47]. Through the intentional design of geometric asymmetry, modulus variation, and impedance discontinuity

16136829, 2026, 36, Downloaded from https://onlinelibrary.wiley.com/doi/10.1002/smll.73728 by Cas-Beijing Institution Of, Wiley Online Library on [29/06/2026]. See the Terms and Conditions (https://onlinelibrary.wiley.com/terms-and-conditions) on Wiley Online Library for rules of use; OA articles are governed by the applicable Creative Commons License

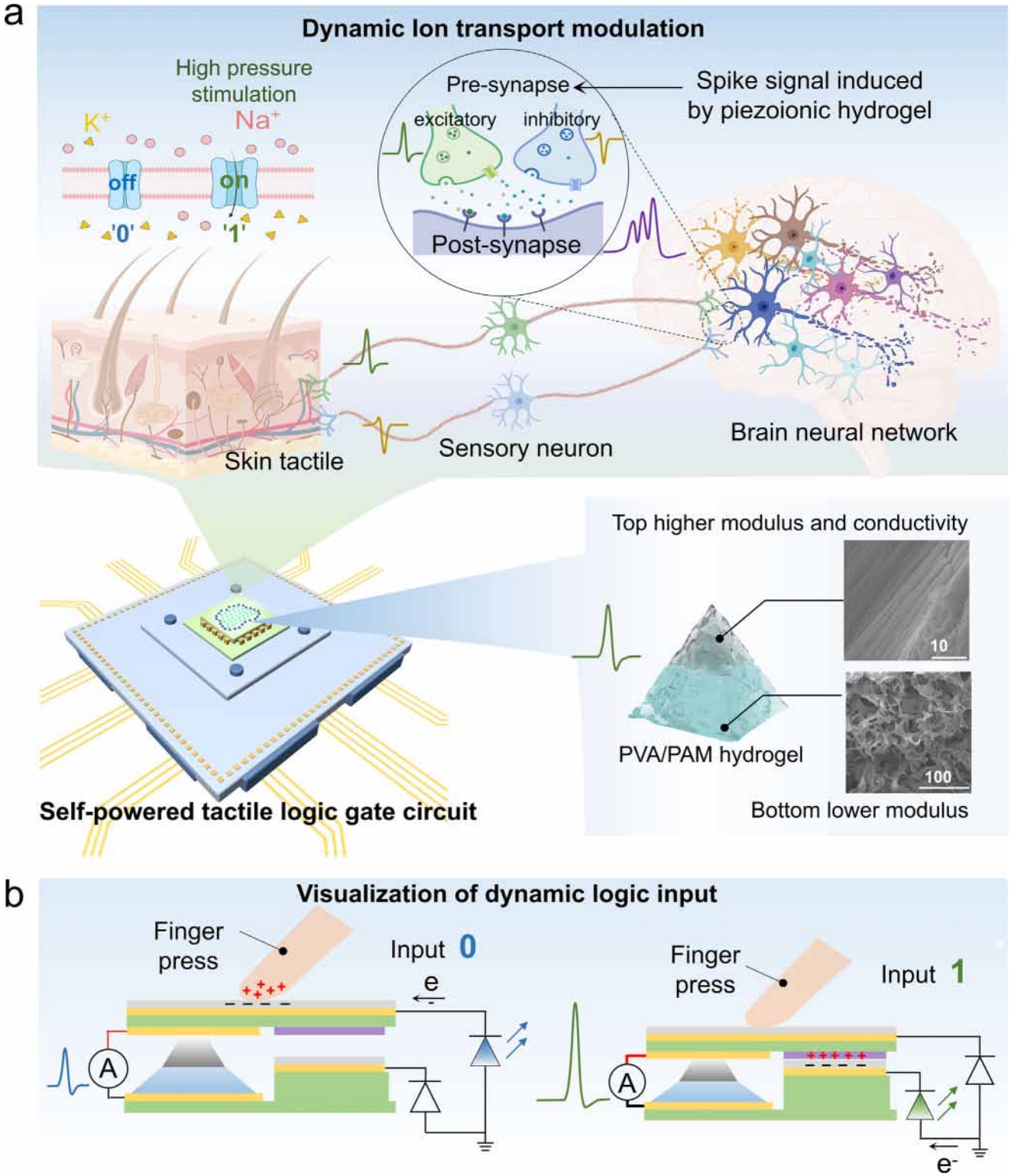


FIGURE 1 | Table of Contents (ToC). (a) Neuromimetic tactile logic gates enabled by asymmetric hydrogel iontronics featuring modulus gradients and impedance discontinuities. Insets show SEM images of hydrogels with different moduli (PVA/PAM 1.5/PEDOT: PSS and PVA/PAM 0.5, respectively), along with a comparison of current outputs between this work and previously reported piezoionic devices. (b) Schematic illustration of the visualization of the dynamic logic process.

16136829, 2026, 36, Downloaded from https://onlinelibrary.wiley.com/doi/10.1002/smll.73728 by Cas-Beijing Institution Of, Wiley Online Library on [29/06/2026]. See the Terms and Conditions (https://onlinelibrary.wiley.com/terms-and-conditions) on Wiley Online Library for rules of use; OA articles are governed by the applicable Creative Commons License

within the hydrogel structure, we developed a hydrogel-based iontronics that exhibits nonlinear current response under compressive strain (noted as ε). This device successfully simulates the processing of excitatory action potentials between neurons, demonstrating its potential for neuron information processing.

The double-network polymer system comprising polyvinyl alcohol (PVA) and polyacrylamide (PAM) was selected as the experimental subject. This combination of soft and rigid double networks has been demonstrated to significantly enhance the mechanical strength of hydrogels [48]. The effect of the geometric asymmetry structure on the electrical output performance of the hydrogel was firstly investigated. A symmetric cube (side length = 10 mm) was used as the control group, while an asymmetric pyramid (side length = 10 mm, height = 10 mm) and a cone (radius = 5 mm, height = 10 mm) served as experimental groups (Figure S1a). The symmetric cube hydrogel exhibited low current and voltage outputs under various compressive strains (ε), displaying a weak alternating current waveform. The maximum short-circuit current ($\boldsymbol{I}_{sc}$) was only about 30 μA (Figure S1b), and the open-circuit voltage ($\boldsymbol{V}_{oc}$) fluctuated between approximately +2 and −2 mV (Figure S2a). When $\varepsilon \geq 60\%$, the current and voltage signals were nearly inverted. The signal reversal under large strain may result from the dominant rebound process occurring upon force release, which reverses the direction of convection. In contrast, both the pyramid and cone structures achieved a $\boldsymbol{V}_{oc}$ of around 20 mV (Figure S2b,c), indicating that asymmetric geometries facilitate the establishment of a potential gradient. Between the two asymmetric designs, the pyramid yielded superior electrical output. At $\varepsilon = 70\%$, the $\boldsymbol{I}_{sc}$ of the pyramid reached approximately 600 μA, compared to about 400 μA for the cone (Figure S1c,d). Therefore, the pyramid-shaped hydrogel was selected for subsequent experiments. Compared to the pyramid structure, the weaker electrical output of the cubic hydrogel likely stems from the challenge of establishing an effective ion convection gradient within its symmetric geometry. To explore this further, we simulated the stress distributions of both hydrogel structures under identical external forces using COMSOL software. The results reveal that the symmetric cube exhibits a uniform stress distribution, while in the pyramid structure, stress is concentrated at the top (Figure S3). This stress concentration facilitates the formation of an effective gradient, thereby enhancing convection efficiency in the pyramid. Darcy's law is commonly applied to characterize the convective transport of electrolyte within hydrogels. The Darcy flow rate provides a quantitative metric for comparing convection intensities between different hydrogel geometries under identical external conditions, thereby offering insight into the resulting ionic current and associated streaming potential. The maximum Darcy velocities for the cubic and pyramidal hydrogels are 2.26×10^{-5} m·s^{-1} and 8.7×10^{-4} m·s^{-1}, respectively (at $\varepsilon \approx 20\%$). This difference becomes more pronounced when ε increases to about 60%, where the maximum Darcy velocities rise to 7.17×10^{-5} m·s^{-1} and 2.7×10^{-3} m·s^{-1}, respectively (Figure S4).

The modulus of the hydrogel was modulated by varying the amount of acrylamide (AM). However, when the AM content was less than 0.5 g, PVA flocculated in a high-concentration NaCl solution (3 M), and a homogeneous solution could only be achieved when the AM amount exceeded 0.5 g (Figure S5). This flocculation behavior is likely due to the Hofmeister effect on PVA, while a sufficient amount of PAM polymer chains can mitigate the interaction between ions and PVA chains [49, 50]. For the low and high modulus experimental groups, PVA/PAM double-network hydrogels were prepared with AM feed amounts of 0.5 and 1.5 g, respectively. The compressive stress–strain curves of the two hydrogels are shown in Figure S6a, both of them remained intact under compression, demonstrating good toughness throughout the testing range. At $\varepsilon = 70\%$, the compressive stress of these two hydrogels was 2.23 and 6.88 MPa, respectively. The compressive modulus of low and high-modulus hydrogels was found to be 0.68 and 24.71 MPa, respectively, calculated from the slopes of the linearly fitted curves within the 0∼30% strain range (Figure S6b). Pyramidal hydrogels with spatial modulus variations were fabricated via sequential precursor polymerization. Firstly, the hydrogel precursor with one modulus was poured into a silicone mold. After it had cured, the second precursor with a different modulus was added. This two-step process resulted in the formation of an integrated bilayer structure. The short-circuit current ($\boldsymbol{I}_{sc}$) and open-circuit voltage ($\boldsymbol{V}_{oc}$) of these modulus gradient iontronic hydrogels were measured under varying ε. Control groups consisted of homogeneous high modulus (HM) and low modulus (LM) hydrogels. Experimental groups included top low modulus with bottom high modulus (TLM-BHM) and top high modulus with bottom low modulus (THM-BLM) (Figure 2a). In both groups, the top layer had a fixed height of 5 mm, and the second precursor was added to form a total height of 10 mm after curing. Experimental results revealed a strongly nonlinear increase in $\boldsymbol{I}_{sc}$ for the THM-BLM group with increasing ε (Figure 2b). At $\varepsilon < 40\%$, $\boldsymbol{I}_{sc}$ remained around 150 μA, lower than other groups. However, once ε reached 60∼70%, $\boldsymbol{I}_{sc}$ increased sharply to approximately 900 μA, significantly exceeding that of the TLM-BHM group. Waveforms of $\boldsymbol{I}_{sc}$ under different ε for all groups are shown in Figure S7. To quantitatively compare the current output behavior across groups, the ratio of current amplitudes at $\varepsilon = 70\%$ and 30% (denoted $\boldsymbol{I}_{70}/\boldsymbol{I}_{30}$) was introduced to evaluate the gating capability. The THM-BLM group exhibited a ratio of 12.2, substantially higher than those of the HM, LM, and TLM-BHM groups (1.49, 3.14, and 1.24, respectively), demonstrating a clear threshold-activated response (Figure 2c). In contrast, $\boldsymbol{V}_{oc}$ values for all groups fluctuated between 20∼35 mV with no obvious gating behavior (Figure S8). A key question is why only the THM-BLM structure exhibits similar ion gating behavior. Non-uniform deformation likely plays a central role. When $\varepsilon \leq 30\%$, the high-modulus top layer in THM-BLM deforms less, resulting in weak ion convection and low current. In contrast, the low-modulus top in TLM-BHM allows greater deformation and higher current at low strain. As ε further increases, deformation propagates throughout the hydrogel. The low-modulus base in THM-BLM undergoes large deformation, while the stiff top resists deformation, leading to stress concentration and enhanced ion convection. Conversely, in TLM-BHM, the high-modulus base restricts further deformation, limiting convection and preventing high current output at large strains. To verify this conjecture, finite element simulations of the THM-BLM and TLM-BHM were conducted using COMSOL. At ε approximately 60%, the maximum Darcy flow velocities for the two structures were found to be 3.9×10^{-4} m·s^{-1} and 4×10^{-6} m·s^{-1}, respectively (Figure 2d). Simultaneously, the pressure distribution was simulated under identical deformation. It was observed that the maximum pressures reached 7×10^4 Pa and 3.2×10^4 Pa, respectively, with more significant stress concentration

16136829, 2026, 36, Downloaded from https://onlinelibrary.wiley.com/doi/10.1002/smll.73728 by Cas-Beijing Institution Of, Wiley Online Library on [29/06/2026]. See the Terms and Conditions (https://onlinelibrary.wiley.com/terms-and-conditions) on Wiley Online Library for rules of use; OA articles are governed by the applicable Creative Commons License

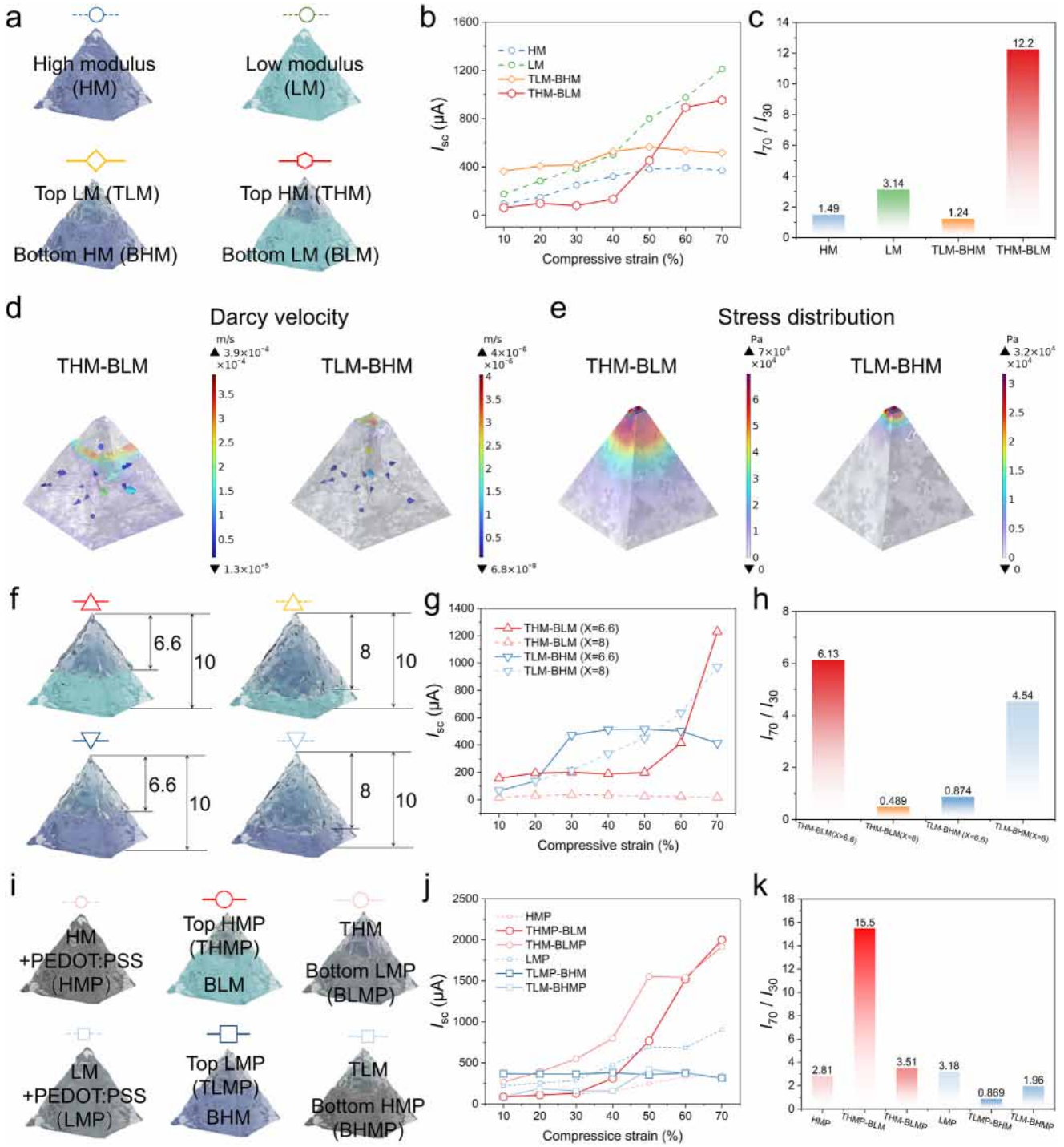


FIGURE 2 | Multi-gradient constructed hydrogel iontronics with gating behavior. (a) Schematic diagram of a pyramid-shaped hydrogel with modulus differences. (b) The short-circuit current (I_{sc}) of hydrogel iontronics with modulus gradient, under different compressive strain (ε). (c) The I_{70}/I_{30} ratio of hydrogel iontronics with different modulus combinations. (d) The Darcy velocity distribution of THM-BLM and TLM-BHM simulated by COMSOL, $\varepsilon \approx 60\%$. (e) The pressure distribution of THM-BLM and TLM-BHM simulated by COMSOL, $\varepsilon \approx 60\%$. (f) Schematic diagram of pyramid-shaped hydrogels with different modulus composition ratios. (g) I_{sc} of hydrogel iontronics with different modulus composition ratios, respectively, $\varepsilon = 10\sim70\%$. (h) The I_{70}/I_{30} ratio of hydrogel iontronics with different modulus composition ratios. (i) Schematic diagram of hydrogel with different composition of PEDOT: PSS. (j) I_{sc} of hydrogel iontronics with different compositions of PEDOT: PSS, $\varepsilon = 10\sim70\%$. (k) The I_{70}/I_{30} ratio of hydrogel iontronics with different composition of PEDOT: PSS. The NaCl was fixed at 3 M in all the above hydrogels.

16136829, 2026, 36, Downloaded from https://onlinelibrary.wiley.com/doi/10.1002/smll.73728 by Cas-Beijing Institution Of, Wiley Online Library on [29/06/2026]. See the Terms and Conditions (https://onlinelibrary.wiley.com/terms-and-conditions) on Wiley Online Library for rules of use; OA articles are governed by the applicable Creative Commons License

appearing at the top of the THM-BLM (Figure 2e). The stress, Darcy velocity, and pressure distributions at about 20% strain are provided in Figure S9. Subsequently, the influence of the relative proportion between high- and low-modulus regions on the electrical output of the hydrogel iontronics was investigated to identify the composition ratios conducive to the gating behavior. Hydrogels with four different modulus composition ratios were prepared (Figure 2f). For both THM-BLM and TLM-BHM configurations, two sets of samples were fabricated with top-layer heights (noted as X) of X = 6.6 mm and X = 8 mm, respectively. The results show that the THM-BLM structure with X = 6.6 mm exhibited a pronounced ionic gating behavior, as evidenced by the strain-dependent change in $\boldsymbol{I}_{sc}$, whereas the group with X = 8 mm showed no significant gating effect (Figure 2g).

The corresponding $\boldsymbol{I}_{sc}$ waveforms under various ε are provided in Figure S10. The $\boldsymbol{I}_{70}/\boldsymbol{I}_{30}$ ratios for the four groups were 6.13, 0.489, 0.874, and 4.54, respectively (Figure 2h). Notably, the $\boldsymbol{I}_{sc}$ of the THM-BLM (X = 6.6 mm) group remained low until ε reached 50%, indicating that the triggering threshold of this iontronics can be modulated by the structural composition. In comparison, the $\boldsymbol{V}_{oc}$ of all groups fluctuated between 20–40 mV with increasing ε, showing no clear trend or gating behavior (Figure S11). The incorporation of PEDOT: PSS into the hydrogel matrix led to a reduction in impedance [51]. This enhancement in conductivity is clearly reflected in the Nyquist plots obtained from electrochemical impedance spectroscopy (EIS) (Figure S12) [52]. The conductivities of the high-modulus hydrogel with and without PEDOT: PSS were measured to be 0.8996 S·cm^{-1} and 0.6557 S·cm^{-1}, respectively, confirming that the addition of a suitable amount of PEDOT: PSS effectively improves the ionic conductivity of the high-modulus hydrogel (Figure S13). Subsequently, the influence of impedance discontinuity on the gating behavior of hydrogel iontronics was investigated. As illustrated in Figure 2i, uniform-modulus hydrogels containing PEDOT: PSS were used as control groups, denoted as HMP and LMP, respectively. Meanwhile, hydrogels with spatially varying modulus and PEDOT: PSS distribution served as experimental groups, labeled as THMP-BLM, THM-BLMP, TLMP-BHM, and TLM-BHMP. The results revealed that the THMP-BLM group exhibited the most pronounced ion gating behavior; the amplitude of the short-circuit current even reached about 2 mA once ε reached 70% (Figure 2j). The $\boldsymbol{I}_{70}/\boldsymbol{I}_{30}$ ratio of THMP-BLM increased to 15.5, significantly higher than those of the other groups (Figure 2k). The corresponding $\boldsymbol{I}_{sc}$ and $\boldsymbol{V}_{oc}$ waveforms are provided in Figures S14 and S15, respectively. Moreover, this $\boldsymbol{I}_{70}/\boldsymbol{I}_{30}$ value exceeds the previously reported value of 12.2 for the THM-BLM group (Figure 2c), demonstrating that introducing impedance discontinuity within the hydrogel structure further enhances the gating performance of the iontronics.

2.2 | Modulating Ion Transport Behavior in Hydrogels

The piezoionic effect in hydrogels refers to the phenomenon wherein deformation induces a mechanical pressure gradient, leading to a potential gradient due to differential mobilities of anions and cations [23]. Investigating the interactions between ions and hydrogel polymer networks offers a pathway to modulate the relative migration rates of anions and cations, which is essential for achieving controllable ion transport in iontronics. Ionic transport behavior within polymer networks is governed by several parameters, such as the ion species, hydrated size, valence state, aggregation state induced by ion concentration, as well as the frequency of the applied mechanical force, among others. These factors shape the operating state of hydrogel iontronics, playing a critical role in enabling functions unattainable in traditional electronics. Accordingly, it is of great significance to discuss the influence of these parameters on the performance of THMP-BLM.

The structure of THMP-BLM hydrogel iontronics is shown in Figure 3a; the corresponding compressive stress under different ε can be seen in Figure S16. Hydrogel iontronics with five kinds of different electrolytes were measured at the same concentration of 0.5 M under ε = 10∼70%. The electrical output performance was demonstrated in Figure 3b,c. The hydrogel iontronics with lithium chloride (LiCl), sodium chloride (NaCl), and calcium chloride ($CaCl_2$) exhibit positive current and voltage signals. When the ε < 40%, the $\boldsymbol{I}_{sc}$ amplitude of LiCl and NaCl hydrogel iontronics was about 25 μA, and the $\boldsymbol{I}_{sc}$ amplitude of $CaCl_2$ hydrogel iontronics was around 15 μA. When $\boldsymbol{\varepsilon}$ reached 70%, the $\boldsymbol{I}_{sc}$ of LiCl and $CaCl_2$ could reach a maximal amplitude of approximately 125 μA. The $\boldsymbol{V}_{oc}$ of these three hydrogel iontronics with different electrolytes fluctuated around -14 mV. However, both lithium nitrate ($LiNO_3$) and sodium nitrate ($NaNO_3$) exhibited negative current and voltage signals. When ε < 40%, the amplitude of $\boldsymbol{I}_{sc}$ of them was below −18 μA and respectively reached the maximum amplitude approximately −128 and −106 μA once $\boldsymbol{\varepsilon}$ reached 70%. The current waveforms of these groups have been shown in Figure S17. With the increase of ε, the $\boldsymbol{V}_{oc}$ of the hydrogel containing $NaNO_3$ fluctuated around −7∼−15 mV. The $\boldsymbol{V}_{oc}$ of $LiNO_3$ showed a gradual increasing trend, from -1 mV at ε = 10% to a maximum of -23 mV at ε = 70%. The detailed waveforms of the $\boldsymbol{V}_{oc}$ of these groups can be seen in Figure S18. This phenomenon of signal formation and reversal may be attributed to the difference in mobilities of ions in the hydrogel network (Figure 3d). At equilibrium, anions and cations are uniformly distributed within the hydrogel matrix (Figure 3d-i). Upon the application of external force, the strain change stimulates the convection flow of the inner solvent water molecules, thereby enabling the migration of the ions. Assuming that the movement rate of anions and cations in the hydrogel is identical to that of the water molecules, the net ionic current would be zero, which is obviously not consistent with the experimental observations.

Based on the theory of the piezoionic effect of hydrogels, the open-circuit potential gradient (∇V) and short-circuit current density (j) can be described by the following formula [23]

$$\nabla V = -\frac{eN\kappa}{\sigma\eta}\frac{D_+}{D_{0+}} - \frac{D_-}{D_{0-}}\nabla P = \alpha\,\nabla P \tag{1}$$

$$j = -\frac{eN\kappa}{\eta}\frac{D_+}{D_{0+}} - \frac{D_-}{D_{0-}}\nabla P = \sigma\,\alpha\,\nabla P \tag{2}$$

where α is the piezoionic coefficient, e is the electronic charge, N is the concentration, κ is the matrix permeability, σ is the conductivity, and η is the fluid viscosity; D_{0+} and D_{0-} are the diffusion coefficients of cations caused by the solution, and D_+

16136829, 2026, 36, Downloaded from https://onlinelibrary.wiley.com/doi/10.1002/smll.73728 by Cas-Beijing Institution Of, Wiley Online Library on [29/06/2026]. See the Terms and Conditions (https://onlinelibrary.wiley.com/terms-and-conditions) on Wiley Online Library for rules of use; OA articles are governed by the applicable Creative Commons License

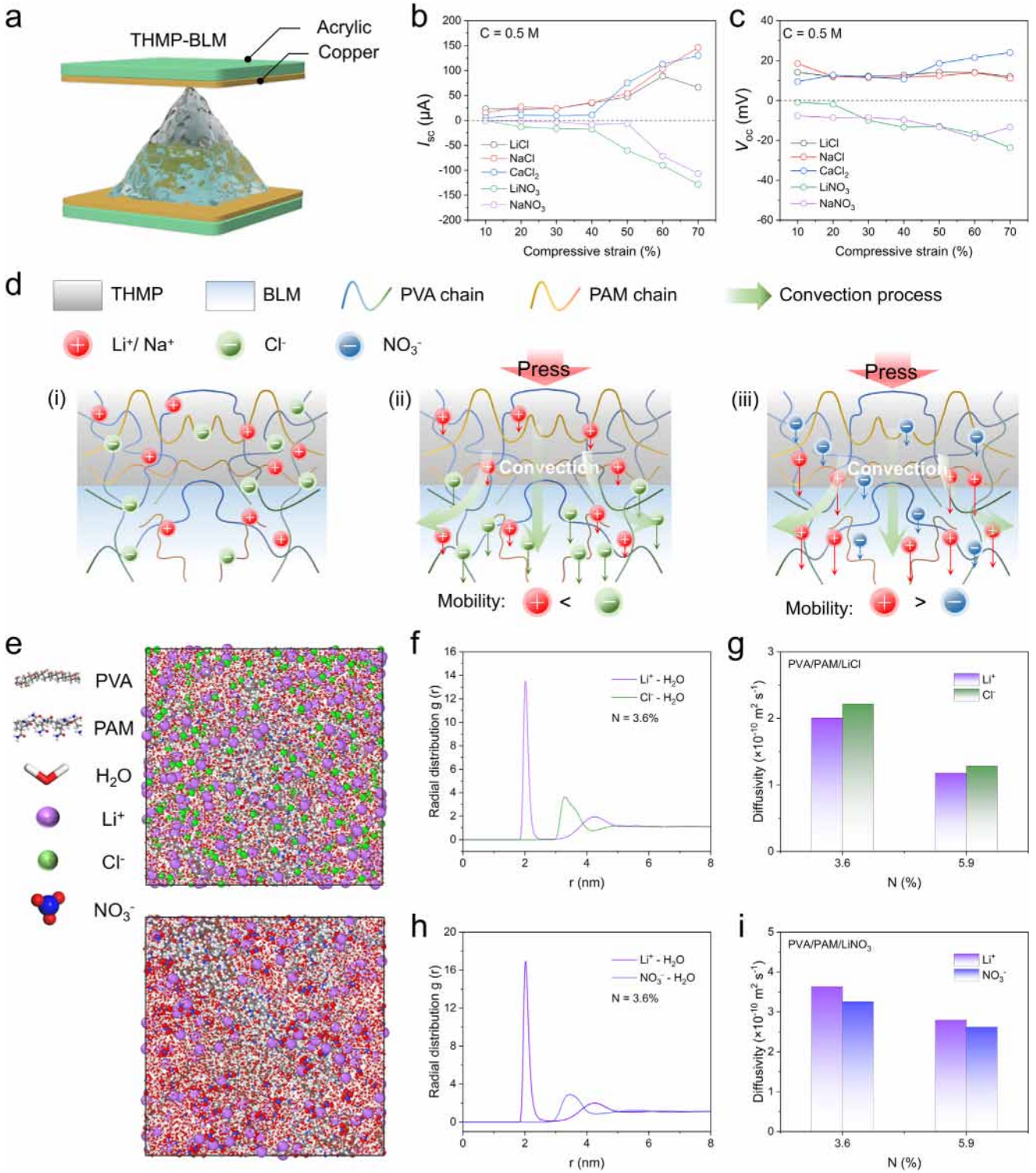


FIGURE 3 | Performance characterization of hydrogel iontronics with different ions in polymer networks. (a) The device structure diagram of THMP-BLM. (b) The short-circuit current ($\boldsymbol{I}_{sc}$) and (c) open-circuit voltage ($\boldsymbol{V}_{oc}$) of THMP-BLM with different kinds of electrolytes under different compressive strains ($\varepsilon = 10\sim70\%$). (d) Schematic diagram of ion convection formation mechanism. (e) Model boxes of PVA/PAM hydrogel with LiCl and $LiNO_3$ for molecular dynamics (MD) simulations. (f) Radial Distribution Functions (RDF) of Li^+—H_2O and Cl^-—H_2O, number percentage (N%) of LiCl = 3.6%. (g) Diffusion coefficients of Li^+ and Cl^- in the polymer matrix under different N% of LiCl. (h) Li^+—H_2O and NO_3^-—H_2O, N = 3.6%. (i) Diffusion coefficients of Li^+ and NO_3^- in the polymer matrix under different N% of $LiNO_3$.

16136829, 2026, 36, Downloaded from https://onlinelibrary.wiley.com/doi/10.1002/smll.73728 by Cas-Beijing Institution Of, Wiley Online Library on [29/06/2026]. See the Terms and Conditions (https://onlinelibrary.wiley.com/terms-and-conditions) on Wiley Online Library for rules of use; OA articles are governed by the applicable Creative Commons License

and D_- are the diffusion coefficients of cations and anions in the hydrogel (Note S1). The mobility of ions in hydrogel is largely determined by their hydration radius; Cl^- (0.332 nm) exhibits a smaller hydration radius than Li^+ (0.382 nm), Na^+ (0.358 nm), and Ca^{2+} (0.412 nm) [53]. Based on the Equations (1) and (2), the positive current and voltage of LiCl, NaCl and $CaCl_2$ may be attributed to the fact that the $D_-(Cl^-)$ is greater than that of $D(Li^+)$, $D(Na^+)$ and $D(Ca^{2+})$ in the PVA/PAM double network hydrogel matrix (Figure 3d-ii) [30, 54]. However, despite NO_3^- (0.335 nm) also having a smaller hydration radius than Li^+ and Na^+, the electrical signal is reversed. The reversal of the electrical signal of $LiNO_3$ and $NaNO_3$ might be attributed to the mobility of $D(NO_3^-)$ is less than that of $D(Li^+)$ and $D(Na^+)$ (Figure 3d-iii). The PVA polymer chains possess a large number of hydroxyl groups; NO_3^- may promote the diffusion ability of Li^+ and Na^+ through a variety of mechanisms, including its weak coordination ability and influence on the solvation structure and hydrogen bond [55, 56]. To verify this hypothesis, we combined the EIS and the cation-selective Au/Nafion composite electrode to examine the conductivity of Na^+ in the hydrogel. The contribution of Na^+ to the total conductivity in two different electrolytes was compared by normalization, thereby indirectly comparing the difference in the diffusion coefficient of Na^+ in the hydrogel (Note S2). The results show that the average contribution of Na^+ to conductivity is 0.199 and 0.282, respectively, which indicates that the Na^+ in $NaNO_3$ might have a higher diffusion coefficient (Figure S19).

Molecular dynamics (MD) simulations were conducted to study ion dynamics in hydrogel systems under various conditions. In particular, we simulated the convective transport behavior of different ions within LiCl- and $LiNO_3$-containing hydrogels under applied pressure (Figure 3e). The radial distribution function (RDF) was employed to analyze the hydration and aggregation states of ions and water molecules inside the hydrogel matrix. The highest intensity peak, observed at $r \approx 2.01$ nm, corresponds to the probability of Li^+ forming a first hydration shell with surrounding water molecules. Under the same number percentage (N = 3.6%), the g(r) values for Li^+—H_2O in the presence of Cl^- and NO_3^- were 13.51 and 16.92, respectively (Figure 3f–h). In PVA/PAM hydrogels with LiCl, the coordination numbers of Li^+ and Cl^- were approximately 2.88 and 7.87, respectively, whereas in those with $LiNO_3$, the values were about 4.20 and 8.34 (Figure S20). The RDF and corresponding coordination numbers for systems with a higher ion number percentage (N = 5.9%) are provided in Figure S21. The mean square displacement (MSD) has been used to calculate the diffusivity of ions at different time points, which is given by the following formula:

$$MSD\ (t) = \left\langle \left| \vec{r_i}(t) - \vec{r_i}(0) \right|^2 \right\rangle \quad (3)$$

where $\vec{r_i}(t)$ is the position of the center of mass of ion (i) at time (t). Upon application of pressure to the hydrogel, anions and cations undergo non-uniform displacement due to convective flow. The MSD curves of these two electrolytes at different number percentages (N) are shown in Figure S22. The diffusion coefficient (D) of the corresponding ions can be calculated by the slope of the MSD curve. $D(Cl^-)$ is greater than $D(Li^+)$ in LiCl-containing hydrogels (Figure 3g). When N = 3.6%, $D(Li^+)$ and $D(Cl^-)$ are 2.00 and 2.22×10^{-10} m^2 s^{-1}, respectively. When N increases to 5.9%, the diffusion coefficients of the two ions are 1.18 and 1.28×10^{-10} m^2 s^{-1}, respectively. Given that the hydration radius of Cl^- is smaller than that of Li^+, Cl^- diffuses more rapidly, which aligns with the experimental observations. In contrast, for hydrogels containing $LiNO_3$, $D(Li^+)$ is generally greater than that of $D(NO_3^-)$ (Figure 3i). When N = 3.6%, $D(Li^+)$ and $D(NO_3^-)$ are 3.63 and 3.26×10^{-10} m^2 s^{-1}, respectively. When N increases to 5.9%, the diffusion coefficients of the two ions are 2.79 and 2.62×10^{-10} m^2 s^{-1}, respectively. This reversal in diffusion behavior may be attributed to the Hofmeister effect between NO_3^- and PVA; NO_3^- changes the hydrogen bond structure of water molecules in the environment [57], thereby accelerating Li^+ diffusion during convection and leading to the observed change in electrical signal.

In addition, NaCl and $LiNO_3$ hydrogels, capable of generating forward and reverse electrical signals, respectively, were selected for investigation to examine the effect of ion concentration on their electrical outputs. The detailed current and voltage waveforms of different NaCl concentrations can be seen in Figures S23 and S24, respectively. As the concentration increased from 1, 2 to 3 M, the maximum current amplitudes of the NaCl hydrogel were approximately 175, 800 and 2000 μA, respectively. The current output exhibited an upward trend with increasing ion concentration. It is speculated that the PVA/PAM hydrogel network is not significantly affected by the increase of Na^+ and Cl^- concentration in the experimental range. Consequently, an elevated NaCl concentration increases the free ion density within the hydrogel, which enhances overall conductivity and thus leads to superior electrical output performance. The amplitude of the $\boldsymbol{V}_{oc}$ was disturbed in the range of 15~25 mV. However, hydrogels with $LiNO_3$ exhibited distinct behaviors. The detailed current and voltage waveforms of different concentrations of $LiNO_3$ can be seen in Figures S25 and S26, respectively. At ε fixed 50%, as the concentration increased from 1 to 2 M and then to 3 M, the maximum $\boldsymbol{I}_{sc}$ reached approximately −88, −41 and −40 μA, respectively. When ε was increased to 70%, the $\boldsymbol{I}_{sc}$ of these groups rose to about −152, −117 and −137 μA, respectively. The decline in $\boldsymbol{I}_{sc}$ with increasing $LiNO_3$ concentration may be attributed to the variation between ions and the polymer network, thereby reducing ion mobility. Specifically, NO_3^- ions act as chaotropes that disrupt the water structure and drive water molecules toward the PVA chains, enhancing the formation of bounding water [57, 58]. This process depletes the free water content within the hydrogel matrix. Consequently, the increased viscosity for ion movement leads to a decrease in the overall output. Meanwhile, the $\boldsymbol{V}_{oc}$ across the three concentration groups showed an increasing trend with greater ε. At $\varepsilon = 70\%$, the $\boldsymbol{V}_{oc}$ of the three groups could reach approximately −45 mV.

The influence of varying external force frequencies on the output voltage of hydrogels containing NaCl and $LiNO_3$ was investigated under a fixed ε of 20%, and the corresponding results are presented in Figure S27. With increasing NaCl concentration, the hydrogel exhibited a progressive decline in peak voltage; conversely, the $LiNO_3$-based hydrogel demonstrated an enhancement. This phenomenon can be attributed to ionic relaxation dynamics. Consequently, the hydrogel iontronics can potentially be used to simulate synaptic plasticity for short-term memory. Furthermore, the cycling durability of hydrogel iontronics was evaluated, and the number of cycles was about 1500 times (as shown in Figure S28). The observed gradual attenuation in current during cyclic loading may result from suppressed secondary

16136829, 2026, 36, Downloaded from https://onlinelibrary.wiley.com/doi/10.1002/smll.73728 by Cas-Beijing Institution Of, Wiley Online Library on [29/06/2026]. See the Terms and Conditions (https://onlinelibrary.wiley.com/terms-and-conditions) on Wiley Online Library for rules of use; OA articles are governed by the applicable Creative Commons License

ion convection caused by accumulated concentration gradients. These gradients drive ion reflux upon reaching equilibrium; however, ionic motion exhibits relaxation behavior, meaning that equilibration of local concentration differences requires finite time. When external compression repeatedly induces convective flow, the ion concentration difference continues to build up, thereby amplifying the inhibitory effect on ion transport. An experiment was designed to validate this hypothesis, as depicted in Figure S29a. When the motor rapidly exerted force on the hydrogel iontronics, the current amplitude exhibits a decay. After interrupting the compression for 30 s, the current signal partially recovers upon reapplication of force. With a longer rest interval of 120 s, the current amplitude is nearly fully restored. The schematic diagram in Figure S29b depicts this ion dynamics process.

2.3 | Bionic Neural Network Logic Circuits Enabled by Hydrogel Iontronics

The inherent separation of storage and computation in the von-Neumann architecture results in extended data access latency, high energy consumption, and significant heat generation [59]. These limitations have motivated the emergence of neuromimetic devices inspired by biological neural networks [60–62]. Although not comparable to the computational power of computers, the human nervous system intrinsically integrates sensing, storage, and processing, thereby enabling low-energy operation and minimizing redundant processes [63]. Unlike digital signal encoding used in conventional computing, biological systems rely on analog signals mediated by ion fluxes during neural activities. Thus, the modulation of such analog signals forms the basis for implementing perception and logical computation in neuromimetic computing devices. Four types of mechano-driven self-powered hydrogel iontronic logic gates were developed by leveraging simple series and parallel configurations of these hydrogel units. We emulate the integration of electrical signals among multiple neurons in a biological network, thereby achieving Boolean logic operations based on ionic spike signals.

The basic requirement of the logic gate circuits is two different states of electrical signals. In this study, the strain of the hydrogel is changed by controlling the stepping distance of the motor to stimulate two kinds of ionic spike current signals with different amplitudes, corresponding to two different electrical signal states, so as to simulate the conduction of ionic electrical signals in the neural network. The excitation of electrical signals between different neurons is achieved by the release of neurotransmitters, and this transmission process requires a certain threshold excitation. Previously, we have successfully prepared hydrogel iontronics with nonlinear ionic current signal output, forming small- and large-amplitude ionic current signals under distinct ε. The current input under small strain and large strain is defined as input '0' and '1', respectively (Figure 4a). The external force can change the synaptic weight of each input hydrogel neural unit, thereby modulating the amplitude of the output ionic current. At the same time, a unified threshold (25 μA) is defined. When the amplitude of the ionic spike current signal exceeds this value, defined as output '1', otherwise, '0'. The truth table of these logic gates has been shown on Figure 4b. Four basic logic gate circuits are realized by simply connecting these hydrogel iontronics in series and parallel, and their voltage signals can be seen as Figure S30. The OR gate is the most basic logic gate, composed of two hydrogel iontronics (NaCl, 1 M) in parallel to simulate the generation of excitation signals. Due to the differences in the impedance of these four hydrogel iontronic logic gates, a 500 Ω resistor is connected in series to uniformly define the output threshold (Figure 4c). The signals without series resistance can be seen in Figure S31. To facilitate the description, the two hydrogel iontronics that make up the input port are marked as A and B, respectively. When input A = B = 1, the peak current amplitude was the largest and exceeded the threshold, then OR (A, B) = 1. If the input A = 1, B = 0 (A = 0 and B = 1), the net peak current amplitude still exceeded the threshold, and the output OR (A, B) = 1. However, if A = B = 0, the current amplitude was lower than the threshold, and the output OR (A, B) = 0 (Figure 4g). A more detailed working mechanism diagram has been shown in Figure S32. The AND gate is built based on the OR structure design idea (Figure 4d). Compared with the OR gate, a hydrogel iontronics containing $NaNO_3$ (0.5 M) was introduced into two parallel hydrogel circuits containing NaCl (1 M) to generate a negative suppression signal (denoted as S1), and the ε was fixed at 20%. To unify the output threshold, a resistor of 300 Ω was connected in parallel to S1. The current and voltage signals without parallel resistors can be seen in Figure S33. When input A = B = 1, the peak current exceeded the threshold, AND (A, B) = 1. When input A = 1, B = 0 (A = 0 and B = 1), the excitation signal was not enough to counteract the suppression signal and AND (A, B) = 0. When the input A = B = 0, the negative current was enhanced, AND (A, B) = 0 (Figure 4h). A more detailed working mechanism diagram can be seen in Figure S34. The NOR gate is modified based on the design of the AND gate. The difference is that two hydrogel iontronics with $NaNO_3$ (0.5 M) are connected in parallel as the input port (Figure 4e). At the same time, another hydrogel iontronics (NaCl, 2 M) was connected in series on the basis of it as the excitation signal emission source (denoted as S2). When the input A = B = 1, the suppression signal was much stronger than the excitation signal, so the net current signal presented a negative current, NOR (A, B) = 0. When the input A = 1, B = 0 (A = 0, B = 1), the suppression signal canceled out part of the excitation signal, and the positive current was enhanced, but its amplitude was not enough to exceed the threshold, so NOR (A, B) = 0. When the input A = B = 0, the suppression signal strength was too low to offset the excitation signal, the forward current was further enhanced, and the amplitude exceeded the threshold. At this time, NOR (A, B) = 1 (Figure 4i). A more detailed working mechanism diagram can be seen in the supporting information (Figure S35). NAND gate is an improvement in NOR circuit design (Figure 4f). Two hydrogel iontronics containing $NaNO_3$ (0.5 M) were still selected in parallel at the input end as a negative suppression signal emission source. A hydrogel iontronics containing NaCl (3 M) was connected in series as an excitation signal emission source (denoted as S3). When the input A = B = 1, the suppression signal greatly weakened the excitation signal emission source, and the current amplitude was lower than the threshold, so the output was 0.When the input end A = 1, B = 0 (A = 0, B = 1), the suppression signal was less than the excitation signal, NAND (A, B) = 1, and the output current amplitude exceeded the threshold, and the output was 1. When the input A = B = 0, the excitation signal reached the maximum, NAND (A, B) = 1, the output was '1' (Figure 4j). A more detailed working mechanism diagram can

16136829, 2026, 36, Downloaded from https://onlinelibrary.wiley.com/doi/10.1002/smll.73728 by Cas-Beijing Institution Of, Wiley Online Library on [29/06/2026]. See the Terms and Conditions (https://onlinelibrary.wiley.com/terms-and-conditions) on Wiley Online Library for rules of use; OA articles are governed by the applicable Creative Commons License

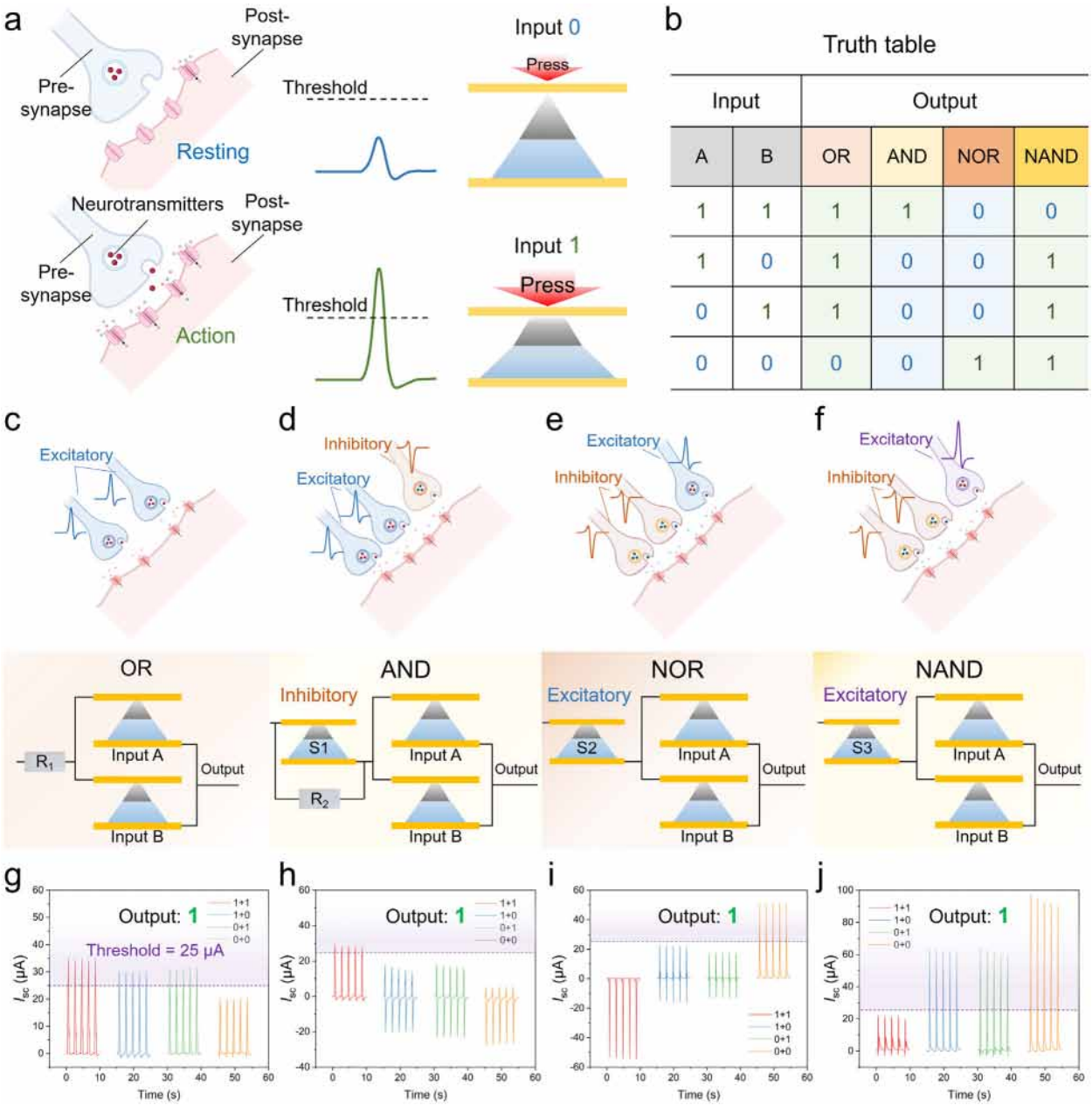


FIGURE 4 | Self-powered bionic neural network logic gate circuits. (a) The ionic current generated by the hydrogel iontronics under small and large strain defined as input '0' and '1', respectively. (b) Truth table of four logic gate circuits. (c-f) The concept diagram and specific circuit structure of the biomimetic neuron network associated with four logic gates, respectively. (g-j) The short-circuit current (I_{sc}) of four hydrogel logic gates under different logical operations (OR, AND, NOR, NAND). Define the output: set the output threshold to 25 μA, and the amplitude of the peak ionic current exceeding the threshold is defined as output '1', otherwise, it is '0'.

be seen in Figure S36. Improving the response speed and working bandwidth is the research focus of this ionic hydrogel logic gate circuit. By improving the rapid transport of ions in the hydrogel and the sensitivity to pressure response, it is expected to improve its performance.

2.4 | Logic-Visualized Hydrogel Iontronics for Advanced Applications

Vision serves as the primary sensory mechanism through which humans acquire external information [64]. It is highly significant to transform abstract Boolean algebra, truth tables, and logical operations into an intuitive process of visualization. Such an approach converts conceptual logical relationships into visual information that is easier for humans to perceive and process. For instance, it allows us to observe how changes in input signals propagate through multi-level logic gates and influence the output, dynamically displaying the signal flow path and the process of logical computation. The visualization of logical operations enables real-time monitoring of equipment functionality, thereby allowing intuitive tracking of computational states. This capability advances the development of HMI in the era of IoT.

16136829, 2026, 36, Downloaded from https://onlinelibrary.wiley.com/doi/10.1002/smll.73728 by Cas-Beijing Institution Of, Wiley Online Library on [29/06/2026]. See the Terms and Conditions (https://onlinelibrary.wiley.com/terms-and-conditions) on Wiley Online Library for rules of use; OA articles are governed by the applicable Creative Commons License

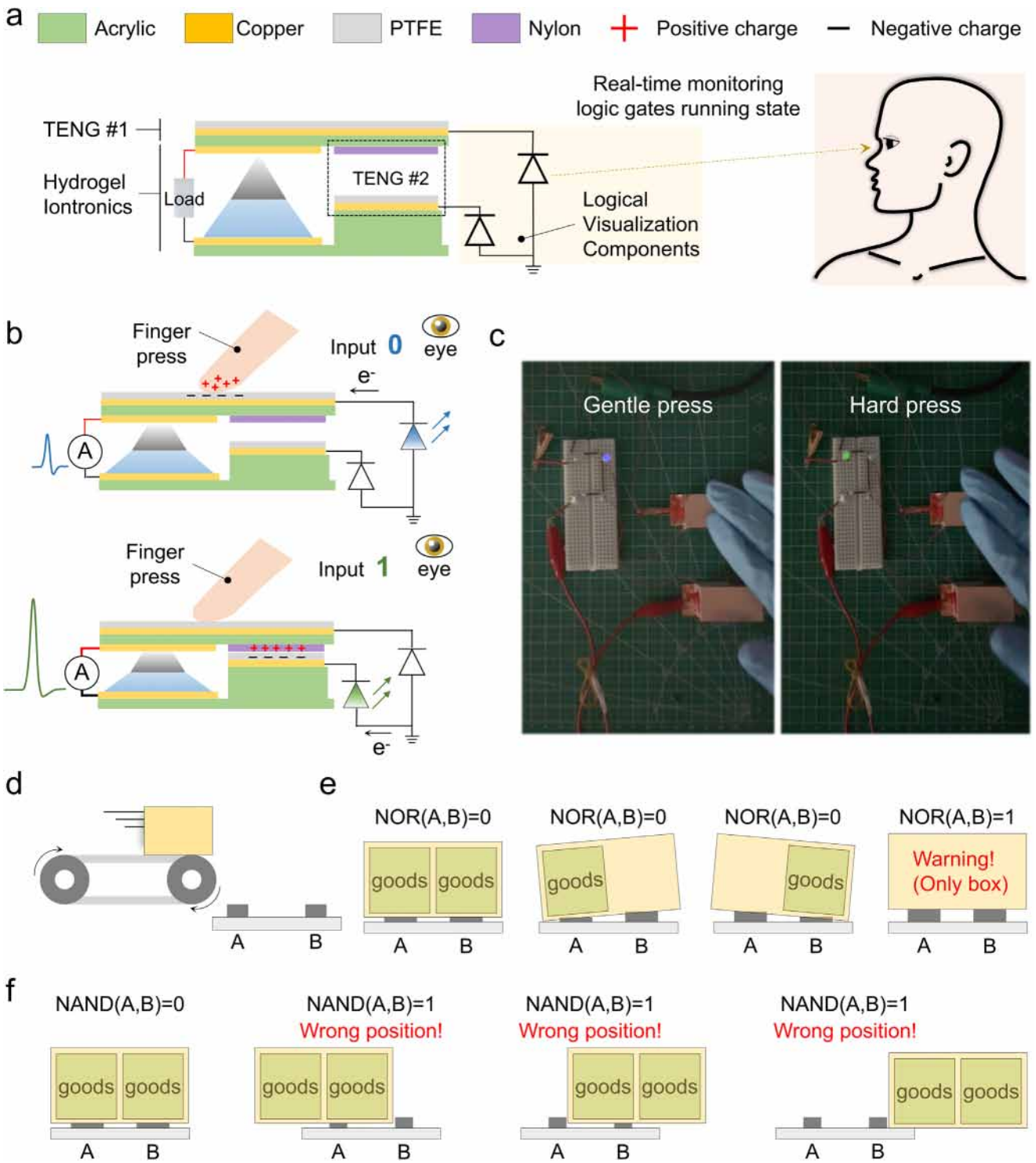


FIGURE 5 | Logic visualization hydrogel iontronic gates and application. (a) The schematic diagram of the structural composition of the logic visualization hydrogel iontronics. (b) The working principle of logic visualization of hydrogel iontronics. (c) The real diagram of logical visualization. (d) The schematic diagram of goods transport scene. (e) The application diagram of NOR gates for screening goods with or without. (f) The application diagram of NAND gates for goods positioning wrong or right.

By integrating triboelectric nanogenerators (TENG) and light-emitting diodes (LED) into this hydrogel iontronics platform, real-time logic-state visualization in fully self-powered hydrogel iontronic logic gates is realized. The specific device architecture is illustrated in Figure 5a. TENG is an energy-harvesting device that converts mechanical energy into electric energy based on the coupled effects of contact electrification and electrostatic induction [65, 66]. The top and middle TENG units are labeled 1 and 2 (denoted as TENG #1 and TENG #2, respectively). A blue and a green LED are connected to represent the input states of '0' and '1', accordingly. The detailed operating mechanism and actual demonstration are depicted in Figure 5b,c, respectively. For TENG

16136829, 2026, 36, Downloaded from https://onlinelibrary.wiley.com/doi/10.1002/smll.73728 by Cas-Beijing Institution Of, Wiley Online Library on [29/06/2026]. See the Terms and Conditions (https://onlinelibrary.wiley.com/terms-and-conditions) on Wiley Online Library for rules of use; OA articles are governed by the applicable Creative Commons License

#1, when fingers contact the PTFE layer (higher electronegativity), electrons exchange occurs, causing fingers to become positively charged and the PTFE surface negatively charged. To balance the interfacial charge, electrons are drawn from the ground to the electrode behind the PTFE due to the electrostatic induction effect, generating a displacement electronic current that illuminates the blue LED. Under light pressure, the hydrogel does not undergo a large strain to excite a weak ionic current. Thus, the blue LED emission corresponds to the input '0'. When greater pressure is applied, the Nylon layer contacts the PTFE film (TENG #2), activating the green LED. Simultaneously, the increased strain triggers the ion-gating threshold of the hydrogel iontronics, resulting in a strong ionic current. Consequently, illumination of the green LED represents the input '1'. This input process of the dynamic logic process has been shown in Video S1. These visualized logic gate circuits can be applied to enable intelligent screening of goods in industrial settings. As illustrated in Figure 5d, goods on a conveyor belt are directed toward the hydrogel iontronic logic gates for automated logical evaluation. As a conceptual demonstration, a NOR gate will be selected to determine whether there are goods in the box. Due to the differential in weight, when a box loaded with goods is transported to the input ports A and B, a logical '1' is registered at each port. At this time, NOR (A, B) = 0, no alarm will be triggered. When the empty box is transported to A and B (A = B = 0), NOR (A, B) = 1, triggering the empty container alarm (Figure 5e). Related demonstration videos can be seen in Video S2. We envision that NAND gates can be applied to determine the position of the box. If input A = B = 1, NAND (A, B) = 0, the position is correct, and the system alarm will not be triggered. Once A and B input ports have any input '0', NAND (A, B) = 1, the system alarm triggers a warning that the goods are not in the right position (Figure 5f). In addition, we believe that these hydrogel iontronic logic gate also has application scenarios in the fields of human-machine interaction, iontronic skin perception, and ionic logic control of mechanical equipment, providing a potential application technology solution for the era of IoT and AI.

3 | Conclusion

This work establishes a self-powered hydrogel iontronic logic architecture that simultaneously achieves ultralow energy consumption, negligible heat dissipation, and in situ information processing. By synergistically engineering geometric asymmetry, modulus contrast, and impedance discontinuity within a PVA/PAM double-network hydrogel, the system exhibits pronounced neuromimetic ion-gating behavior that faithfully reproduces neuronal subthreshold responses and action-potential-like ionic spikes under mechanical stimulation. The optimized THMP-BLM configuration delivers state-of-the-art performance, achieving an I_{70}/I_{30} ratio of 15.5 and peak ionic current densities approaching ~2 mA cm^{-2} at 70% compressive strain (ε), corresponding to a sensitivity of 0.275 A m^{-2} kPa^{-1}, orders of magnitude higher than conventional and times higher than advanced piezoionic systems. Distinct electrolytes give rise to well-defined and programmable electrical polarities: LiCl, NaCl, and $CaCl_2$ generate positive current and voltage signals, whereas $LiNO_3$ and $NaNO_3$ produce reversed outputs. Molecular dynamics simulations reveal that specific NO_3^-—water interactions invert diffusion asymmetry within the hydrogel network, providing a mechanistic origin for electrolyte-programmable excitatory and inhibitory ionic transport. Through simple series-parallel interconnection, these hydrogel iontronic units emulate neuronal signal integration. In the THMP-BLM configuration, the positive ionic current obtained in NaCl and the negative current obtained in $NaNO_3$ directly map onto excitatory and inhibitory synaptic responses, respectively, rendering both the gating threshold and signal polarity deterministically programmable via electrolyte selection. On this basis, four fundamental self-powered Boolean logic gates (OR, AND, NOR, and NAND) are realized using purely mechano-induced ionic spikes, enabling autonomous tactile logic operation for neuromorphic signal processing. Coupling the hydrogel iontronics with TENG enables real-time, color-resolved visualization of logic states, directly linking tactile input to readable logical output. Together, this work advances hydrogel iontronics from passive sensing toward integrated perception-cognition, providing a new technological framework for neuromorphic HMIs and next-generation IoT systems.

4 | Methods

4.1 | Materials

Polyvinyl alcohol (PVA-224, 99%, M_w = 205000, Aladdin). Acrylamide (AM, 99%), Methylene-bis-acrylamide (MBAA, 99%), Ammonium persulphate (APS, 99%), Sodium chloride (NaCl, 99%), Lithium chloride (LiCl, 99%), Calcium chloride ($CaCl_2$, 99%), Lithium nitrate ($LiNO_3$, 99%), Sodium nitrate ($NaNO_3$, 99%) all purchased from Macklin and used as received. Poly(3,4-ethylenedioxythiophene)-poly(styrene sulfonate) (PEDOT: PSS, 1.3 wt.% dispersion in H_2O, conductive grade) was purchased from Aldrich and used as received.

4.2 | Preparation of PVA/PAM Hydrogel

PVA-224 was added into deionized water and stirred at 90°C for about 2 h to obtain a homogeneous solution (50 mg mL^{-1}). The above-mentioned PVA aqueous solution was taken 4 mL and diluted by D.I. water to a total volume of the solution (5 mL). When prepared hydrogel with PEDOT: PSS, 1 mL PEDOT: PSS solution was added to PVA aqueous solution (4 mL, 50 mg mL^{-1}) under stirring to the total volume of the solution (5 mL). AM (0.5 g or 1.5 g for different modulus, monomer), MBAA (10 mg, cross-linker), and APS (50 mg, initiator) were added to the above solution, respectively. The salt was weighed according to the corresponding concentration, stirred at room temperature, and placed in a refrigerator at 4°C. The above solution was added to the silicone mold, and it was heated in the oven at 60°C for 20–30 min. After curing, it was taken out and used for subsequent experiments.

4.3 | Fabrication of Hydrogel Iontronics

The copper electrode was fixed on the acrylic board by double-sided adhesive. The hydrogel was located on it to ensure that there were no bubbles between the hydrogel and the electrode, so as to avoid the capacitance change of the electrode interface caused by insufficient contact. Then, the upper and lower copper electrodes

16136829, 2026, 36, Downloaded from https://onlinelibrary.wiley.com/doi/10.1002/smll.73728 by Cas-Beijing Institution Of, Wiley Online Library on [29/06/2026]. See the Terms and Conditions (https://onlinelibrary.wiley.com/terms-and-conditions) on Wiley Online Library for rules of use; OA articles are governed by the applicable Creative Commons License

and the hydrogel were fixed by 3 M tape to form a sandwich structure.

4.4 | Characterization and Measurements

The morphology of the hydrogel network with different modulus was photographed by scanning electron microscopy (SEM, SU8020, Hitachi) with the 5.0 kV accelerating voltage after freeze-drying treatment. A step motor (Linear Motion 1100) was used to provide the input of mechanical motions. Signals were collected by a test system consisting of an electrometer (6514, Keithley, USA) and a data acquisition card (BNC-2120, National Instruments, USA). All electrochemical properties were carried out by electrochemical workstation (Multi Auto-lab M204). Electrochemical impedance spectroscopy (EIS) was measured in the range of 0.1 MHz to 1 Hz.

4.5 | Finite Element Analysis

The finite element simulations were performed using COMSOL Multiphysics 6.2, coupling three modules: Solid Mechanics, Darcy's Law, and Tertiary Current Distribution. In the model, the convection term in the Tertiary Current Distribution module is driven by the Darcy velocity field, while the Darcy's Law and Solid Mechanics modules are coupled through a poroelastic multiphysics interface. The material parameters of the hydrogel were determined experimentally and are provided in the Supplementary Materials (The simulation parameters for analyzing shape differences were density 1.1 kg/m^3, viscosity 1 Pa·s, porosity 0.8 and 0.4, Young's modulus 1×10^4 and 2×10^4 Pa, relative permittivity 78, Poisson's ratio 0.46, and permeability $1{\times}10^{-10}$ m^2. In the Solid Mechanics module, the bottom surface of the hydrogel was fixed, while a normal pressure of 28 mN was applied to the top surfaces of both hydrogels. The pressure field for the Darcy flow was obtained from the results of the Solid Mechanics module, with gravitational acceleration applied in the negative Z direction. Regarding the electrolyte potential, only a quantitative analysis was performed due to numerical precision limits. The hydrogel, modeled as a porous electrode, was grounded at the bottom, allowing ionic current to flow out through the bottom surface.

4.6 | MD Simulations

Molecular dynamics (MD) simulations were carried out to explore microscopic mechanisms for different current responses to concentration in LiCl and $LiNO_3$ hydrogels. Initial configurations are constructed by randomly placing 3 polyvinyl alcohol (PVA) polymers (705 atoms per polymer), 50 pre-polymerized short polyacrylamide (SPAM) chains (102 atoms per chain), and 25 methylene-bis-acrylamide (MBAA) in simulation cells using software PACKMOL. MBAA and SPAM are crosslinked to construct 3D-network structures. Subsequently, 3600 water molecules and ions (Li^+, Cl^-, and NO_3^-) are randomly inserted in models, and the number of ions (Table S2) are adjusted for different concentrations. Water molecules are numerically described by the SPC/E model. The optimized potentials for liquid simulations all-atom (OPLS-AA) force field is applied is describe the interactions among other particles.

These models are relaxed through a process with two stages. In the first stage, long-range electrostatic interactions are not considered to avoid numerical errors induced by the drastic density change. At first, MD simulations are performed at 20 K within the NVT (number, volume, and temperature) ensemble for 25 ps. Then, all models are relaxed at 300 K for 500 ps in the NPT (number, pressure, temperature) ensemble under 1 bar. In the second stage, long-range electrostatic interactions are considered through the particle-particle particle-mesh (PPPM) method with a relative force error of 10^{-4}. Simulation models are relaxed at 300 K for 150 ps and heated to 450 K within 150 ps. After a relaxation for 200 ps at 450 K, they are gradually cooled to 300 K within 150 ps and equilibrated at 300 K for another 250 ps to obtain fully relaxed structures. All simulations in the second stage are performed using the *NPT* ensemble. With fully relaxed models, we carry out a 200 ps *NVT* simulation at 300 K to reach equilibrium. Eventually, a 600 ps *NVE* (number, pressure, energy) simulation is conducted to sample MD trajectories for mean square displacement (MSD) and diffusion coefficient. MSD is calculated in software kinisi with a correlation time of 100 ps, whose slope in the last 50 ps is used to obtain the diffusion coefficient. Another 200 ps *NVE* simulation is conducted, with the last 100 ps for the radius distribution function (RDF) and coordination number. All MD simulations are performed using software Large-scale Atomic/Molecular Massively Parallel Simulator (LAMMPS). 9 and 11 Å are used as the cut-off distances for van der Waals and electrostatic interactions, respectively. The timestep is set as 0.5 fs.

Author Contributions

D.W. and Z. L. W. supervised the whole project. Y.W.O.Y. and X.X. have contributed equally to this article. Y.W.O.Y. designed and carried out all of the experiments in this paper and analyzed the corresponding data. X. X. carried out all of the molecular dynamics simulations. Y. G. Z. supervised the molecular dynamics simulation process. Y. Y. Z. finished the theoretical modeling of COMSOL. X. L. supported part of the data analysis. All the authors discussed the results and commented on the manuscript. D.W. and Y.W.O.Y. wrote this paper.

Acknowledgements

This work was supported by the National Natural Science Foundation (Grant No. 22479016) and China Postdoctoral Science Foundation (certificate No. 2025M781041). Thanks to Puguang Peng for the help with the SEM.

Conflicts of Interest

The authors declare no competing interests.

Data Availability Statement

The data that support the findings of this study are available from the corresponding author upon reasonable request.

References

1. H. Chun and T. D. Chung, "Iontronics," *Annual Review of Analytical Chemistry* 8 (2015): 441–462, https://doi.org/10.1146/annurev-anchem-071114-040202.

16136829, 2026, 36, Downloaded from https://onlinelibrary.wiley.com/doi/10.1002/smll.73728 by Cas-Beijing Institution Of, Wiley Online Library on [29/06/2026]. See the Terms and Conditions (https://onlinelibrary.wiley.com/terms-and-conditions) on Wiley Online Library for rules of use; OA articles are governed by the applicable Creative Commons License

2. D. Wei, F. Yang, Z. Jiang, and Z. Wang, "Flexible Iontronics Based on 2D Nanofluidic Material," *Nature Communications* 13 (2022): 4965, https://doi.org/10.1038/s41467-022-32699-x.

3. X. Li, R. Li, S. Li, Z. L. Wang, and D. Wei, "Triboiontronics With Temporal Control of Electrical Double Layer Formation," *Nature Communications* 15 (2024): 6182, https://doi.org/10.1038/s41467-024-50518-3.

4. H. Daiguji, P. D. Yang, and A. Majumdar, "Ion Transport in Nanofluidic Channels," *Nano Letters* 4 (2004): 137–142, https://doi.org/10.1021/nl0348185.

5. R. B. Schoch, J. Y. Han, and P. Renaud, "Transport Phenomena in Nanofluidics," *Reviews of Modern Physics* 80 (2008): 839–883, https://doi.org/10.1103/RevModPhys.80.839.

6. D. K. Kim, C. H. Duan, Y. F. Chen, and A. Majumdar, "Power Generation From Concentration Gradient by Reverse Electrodialysis in Ion-Selective Nanochannels," *Microfluidics and Nanofluidics* 9 (2010): 1215–1224, https://doi.org/10.1007/s10404-010-0641-0.

7. A. Wang, C. Breakwell, F. Foglia, et al., "Selective Ion Transport Through Hydrated Micropores in Polymer Membranes," *Nature* 635 (2024): 353–358, https://doi.org/10.1038/s41586-024-08140-2.

8. Y. Dai, C. F. Chamberlayne, M. S. Messina, et al., "Interface of Biomolecular Condensates Modulates Redox Reactions," *Chemistry* 9 (2023): 1594–1609, https://doi.org/10.1016/j.chempr.2023.04.001.

9. H. Qian, D. Wei, and Z. Wang, "Bionic Iontronics Based on Nano-Confined Structures," *Nano Research* 16 (2023): 11718–11730, https://doi.org/10.1007/s12274-023-5705-z.

10. X. Li, Y. Wei, X. Gao, Z. Zhang, Z. L. Wang, and D. Wei, "Harnessing Triboiontronic Maxwell's Demon by Triboelectric-Induced Polarization for Efficient Energy-Information Flow," *Joule* 9 (2025): 101888, https://doi.org/10.1016/j.joule.2025.101888.

11. F. Y. Yang, P. G. Peng, Z. Y. Yan, et al., "Vertical Iontronic Energy Storage Based on Osmotic Effects and Electrode Redox Reactions," *Nature Energy* 9 (2024): 263–271, https://doi.org/10.1038/s41560-023-01431-4.

12. Y. Ouyang, X. Li, S. Li, et al., "Opto-Iontronic Coupling in Triboelectric Nanogenerator," *Nano Energy* 116 (2023): 108796, https://doi.org/10.1016/j.nanoen.2023.108796.

13. D. Hassabis, D. Kumaran, C. Summerfield, and M. Botvinick, "Neuroscience-Inspired Artificial Intelligence," *Neuron* 95 (2017): 245–258, https://doi.org/10.1016/j.neuron.2017.06.011.

14. D. Marković, A. Mizrahi, D. Querlioz, and J. Grollier, "Physics for Neuromorphic Computing," *Nature Reviews Physics* 2 (2020): 499–510, https://doi.org/10.1038/s42254-020-0208-2.

15. S. Dai, X. Liu, Y. Liu, et al., "Emerging Iontronic Neural Devices for Neuromorphic Sensory Computing," *Advanced Materials* 35 (2023): 2300329, https://doi.org/10.1002/adma.202300329.

16. J. Yan, J. P. K. Armstrong, F. Scarpa, and A. W. Perriman, "Hydrogel-Based Artificial Synapses for Sustainable Neuromorphic Electronics," *Advanced Materials* 36 (2024): 2403937, https://doi.org/10.1002/adma.202403937.

17. T. Mei, W. Liu, G. Xu, et al., "Ionic Transistors," *ACS Nano* 18 (2024): 4624–4650, https://doi.org/10.1021/acsnano.3c06190.

18. J. Rivnay, S. Inal, A. Salleo, R. M. Owens, M. Berggren, and G. G. Malliaras, "Organic Electrochemical Transistors," *Nature Reviews Materials* 3 (2018): 17086, https://doi.org/10.1038/natrevmats.2017.86.

19. W. Liu, T. Mei, Z. Cao, et al., "Bioinspired Carbon Nanotube–Based Nanofluidic Ionic Transistor With Ultrahigh Switching Capabilities for Logic Circuits," *Science Advances* 10 (2024): adj7867, https://doi.org/10.1126/sciadv.adj7867.

20. Y. Zhang, C. M. J. Tan, C. N. Toepfer, X. Lu, and H. Bayley, "Microscale Droplet Assembly Enables Biocompatible Multifunctional Modular Iontronics," *Science* 386 (2024): 1024–1030, https://doi.org/10.1126/science.adr0428.

21. E. M. Ahmed, "Hydrogel: Preparation, Characterization, and Applications: A Review," *Journal of Advanced Research* 6, no. 6 (2015): 105–121, https://doi.org/10.1016/j.jare.2013.07.006.

22. C. Keplinger, J.-Y. Sun, C. C. Foo, P. Rothemund, G. M. Whitesides, and Z. Suo, "Stretchable, Transparent, Ionic Conductors," *Science* 341 (2013): 984–987, https://doi.org/10.1126/science.1240228.

23. Y. Dobashi, D. Yao, Y. Petel, et al., "Piezoionic Mechanoreceptors: Force-Induced Current Generation in Hydrogels," *Science* 376 (2022): 502–507, https://doi.org/10.1126/science.aaw1974.

24. K. Chen and D. Ho, "Piezoionics: Mechanical-to-Ionic Transduction for Sensing, Biointerface, and Energy Harvesting," *Aggregate* 5 (2024): 425.

25. M. Hu, J. Ren, Y. Pan, et al., "Scaled Elastic Hydrogel Interfaces for Brain Electrophysiology," *Advanced Functional Materials* 34 (2024): 2407926, https://doi.org/10.1002/adfm.202407926.

26. W. U. Khan, Z. Shen, S. M. Mugo, H. Wang, and Q. Zhang, "Implantable Hydrogels as Pioneering Materials for Next-Generation Brain–Computer Interfaces," *Chemical Society Reviews* 54 (2025): 2832–2880, https://doi.org/10.1039/D4CS01074D.

27. Y. Sun, G. Tian, T. Yang, et al., "Crosslinking-Modulated Hydrogel Piezoionic Sensor for Pattern Security Authentication in Human-Machine Interfaces," *Advanced Functional Materials* 35 (2025): 2420187, https://doi.org/10.1002/adfm.202420187.

28. F. Li, X. Cai, G. Liu, H. Xu, and W. Chen, "Piezoionic SnSe Nanosheets-Double Network Hydrogel for Self-Powered Strain Sensing and Energy Harvesting," *Advanced Functional Materials* 33 (2023): 2300701, https://doi.org/10.1002/adfm.202300701.

29. L. Jia, L. Li, Z. H. Guo, et al., "Giant Iontronic Flexoelectricity in Soft Hydrogels Induced by Tunable Biomimetic Ion Polarization," *Advanced Materials* 36 (2024): 2403830, https://doi.org/10.1002/adma.202403830.

30. H. Liu, X. Ji, Z. Guo, et al., "A High-Current Hydrogel Generator With Engineered Mechanoionic Asymmetry," *Nature Communications* 15 (2024): 1494, https://doi.org/10.1038/s41467-024-45931-7.

31. Y. Li, H. Yin, C. Jiang, et al., "Rapid Fabrication of Antifreezing Piezoionic Hydrogels for Fast Charging and Enhanced Energy Harvesting Frequency via Ion-Regulating Nanoparticles," *Advanced Functional Materials* 36 (2025): 15804.

32. W. Zhu, B. Wu, Z. Lei, and P. Wu, "Piezoionic Elastomers by Phase and Interface Engineering for High-Performance Energy-Harvesting Ionotronics," *Advanced Materials* 36 (2024): 2313127, https://doi.org/10.1002/adma.202313127.

33. W. Chen, S. Zhang, A. Zhang, et al., "Intercellular Ion-Gradient Piezoheterogated Biphasic Gel for Ultrahigh Iontronic Generation," *Journal of the American Chemical Society* 147 (2025): 3283–3292, https://doi.org/10.1021/jacs.4c13305.

34. L. Li, Y. Shao, L. Jia, et al., "A d33 Piezoionic Hydrogel with Bioinspired Multi-Gradient Structure for Enhanced Mechano-Iontronic Transduction," *Nano Energy* 133 (2025): 110477.

35. J. Dai, Y. Xue, X. Chen, et al., "Artificial Nerve for Neuromodulation Based on Structured Piezoionic Hydrogel," *Device* 2 (2024): 100436.

36. S. Wang, T. Yang, D. Zhang, Q. Hua, and Y. Zhao, "Unveiling Gating Behavior in Piezoionic Effect: Toward Neuromimetic Tactile Sensing," *Advanced Materials* 36 (2024): 2405391, https://doi.org/10.1002/adma.202405391.

37. B. Sun, T. Guo, G. D. Zhou, et al., "Synaptic Devices Based Neuromorphic Computing Applications in Artificial Intelligence," *Materials Today Physics* 18 (2021): 100393, https://doi.org/10.1016/j.mtphys.2021.100393.

38. N. Raeis-Hosseini and J.-S. Lee, "Controlling the Resistive Switching Behavior in Starch-Based Flexible Biomemristors," *ACS Applied Materials & Interfaces* 8 (2016): 7326–7332, https://doi.org/10.1021/acsami.6b01559.

39. Y. Park and J. S. Lee, "Flexible Multistate Data Storage Devices Fabricated Using Natural Lignin at Room Temperature," *ACS Applied*

16136829, 2026, 36, Downloaded from https://onlinelibrary.wiley.com/doi/10.1002/smll.73728 by Cas-Beijing Institution Of, Wiley Online Library on [29/06/2026]. See the Terms and Conditions (https://onlinelibrary.wiley.com/terms-and-conditions) on Wiley Online Library for rules of use; OA articles are governed by the applicable Creative Commons License

Materials & Interfaces 9 (2017): 6207–6212, https://doi.org/10.1021/acsami.6b14566.

40. M. Torbati, K. Mozaffari, L. P. Liu, and P. Sharma, "Coupling of Mechanical Deformation and Electromagnetic Fields in Biological Cells," *Reviews of Modern Physics* 94 (2022): 025003, https://doi.org/10.1103/RevModPhys.94.025003.

41. H. Tian, C. Wang, Y. Chen, et al., "Optically Modulated Ionic Conductivity in a Hydrogel for Emulating Synaptic Functions," *Science Advances* 9 (2023): add6950, https://doi.org/10.1126/sciadv.add6950.

42. Y. Kim, A. Chortos, W. Xu, et al., "A Bioinspired Flexible Organic Artificial Afferent Nerve," *Science* 360 (2018): 998–1003, https://doi.org/10.1126/science.aao0098.

43. Y. Long, B. Zhao, M. Liu, W. Hu, and X. Pu., "Smart Hydrogel Tactile Sensors and Systems: A Comprehensive Review," *SmartSys* 1 (2025): 70015.

44. A. Wang, S. Feng, T. Xiao, et al., "Microenvironment-Engineered Piezoionic Hydrogel Nanogenerators for Enhanced Energy Harvesting and Sensing," *SmartSys* 1 (2025): 70004.

45. Z. Sun, T. He, Z. Ren, et al., "Moving Toward Human-Like Perception and Sensation Systems—From Integrated Intelligent Systems to Decentralized Smart Devices," *SmartSys* 1 (2025): 4.

46. J. Yin, P. Jia, Z. Ren, et al., "Recent Advances in Self-Powered Sensors Based on Ionic Hydrogels," *Research* 8 (2025): 0571, https://doi.org/10.34133/research.0571.

47. H. Ma, S. Li, S. Wang, W. Yang, and J. Han, "Biomimetic All-Wood Sponge for the Co-Generation of Adsorption-Based Atmospheric Water Harvesting and Hydrovoltaic Power Generation," *Research* 9 (2026): 1195, https://doi.org/10.34133/research.1195.

48. J. P. Gong, Y. Katsuyama, T. Kurokawa, and Y. Osada, "Double-Network Hydrogels with Extremely High Mechanical Strength," *Advanced Materials* 15 (2003): 1155–1158, https://doi.org/10.1002/adma.200304907.

49. Z. He, Y. Chen, J. Li, J. Qu, L. Chen, and F. Li, "*Hofmeister* Effect Regulated Gel Iontronic Sensors for Wide-Range Pressure Perception," *The Innovation Materials* 2 (2024): 100078, https://doi.org/10.59717/j.xinnmater.2024.100078.

50. J. Li, J. Li, Y. Tang, et al., "Touchable Gustation via a Hoffmeister Gel Iontronic Sensor," *ACS Nano* 17 (2023): 5129–5139, https://doi.org/10.1021/acsnano.3c00516.

51. Y.-W. Kim, J.-M. Park, C. S. Park, et al., "Anisotropically Conductive Hydrogels with Directionally Aligned PEDOT:PSS in a PVA Matrix," *ACS Applied Materials & Interfaces* 16 (2024): 4013–4023, https://doi.org/10.1021/acsami.3c16094.

52. V. Amoli, J. S. Kim, E. Jee, et al., "A Bioinspired Hydrogen Bond-Triggered Ultrasensitive Ionic Mechanoreceptor Skin," *Nature Communications* 10 (2019): 4019, https://doi.org/10.1038/s41467-019-11973-5.

53. E. Nightingale Jr, "Phenomenological Theory of Ion Solvation. Effective Radii of Hydrated Ions," *The Journal of Physical Chemistry* 63 (1959): 1381–1387, https://doi.org/10.1021/j150579a011.

54. B. Chen, J. Feng, Q. Chen, et al., "Specific Behavior of Transition Metal Chloride Complexes for Achieving Giant Ionic Thermoelectric Properties," *npj Flexible Electronics* 6 (2022): 79, https://doi.org/10.1038/s41528-022-00213-4.

55. W. Wahyudi, V. Ladelta, L. Tsetseris, et al., "Lithium-Ion Desolvation Induced by Nitrate Additives Reveals New Insights Into High Performance Lithium Batteries," *Advanced Functional Materials* 31 (2021): 2101593, https://doi.org/10.1002/adfm.202101593.

56. Y. H. Liang, W. B. Wu, D. P. Li, et al., "Highly Stable Lithium Metal Batteries by Regulating the Lithium Nitrate Chemistry with a Modified Eutectic Electrolyte," *Advanced Energy Materials* 12 (2022): 2202493, https://doi.org/10.1002/aenm.202202493.

57. N. P. Lo and B. W. Ninham, "Hofmeister Phenomena: an Update on Ion Specificity in Biology," *Chemical Reviews* 112 (2012): 2286.

58. S. Wu, M. Hua, Y. Alsaid, et al., "Poly(Vinyl Alcohol) Hydrogels With Broad-Range Tunable Mechanical Properties via the Hofmeister Effect," *Advanced Materials* 33 (2021): 2007829, https://doi.org/10.1002/adma.202007829.

59. W. Chen, L. Zhai, S. Zhang, et al., "Cascade-Heterogated Biphasic Gel Iontronics for Electronic-to-Multi-Ionic Signal Transmission," *Science* 382 (2023): 559–565, https://doi.org/10.1126/science.adg0059.

60. X. Zhu, Z. Wu, and Z. Zhao, "Bio-Inspired Heterointerfacial Ion-Gating and Iontronic Neuromorphics," *Iontronics* 1 (2025): 4, https://doi.org/10.20517/iontronics.2025.04.

61. B. Xie and P. Yu, "Ion-Shuttling Memristor: Towards Ionic Computing and Neuromorphic Sensing," *Iontronics* 2 (2026): 2, https://doi.org/10.20517/iontronics.2026.02.

62. Z. Wang, Y. Zhang, B. Yang, et al., "The Road Ahead for Hydrogel Electrolytes in Aqueous Zinc Metal Batteries," *Iontronics* 2 (2026): 16.

63. Z. Y. Lei and P. Y. Wu, "Short-Term Plasticity, Multimodal Memory, and Logical Responses Mimicked in Stretchable Hydrogels," *Matter* 6 (2023): 429.

64. P. Peng, P. Shen, H. Qian, et al., "Photochemical Iontronics With Multitype Ionic Signal Transmission at Single Pixel for Self-Driven Color and Tridimensional Vision," *Device* 3 (2025): 100574, https://doi.org/10.1016/j.device.2024.100574.

65. Z. L. Wang, T. Jiang, T. Ma, and R. Yang, "Nanogenerators for Blue Energy," *MRS Bulletin* 50 (2025): 450–458.

66. Z. L. Wang, X. Wang, S.-W. Kim, and R. Zhang, "Nanogenerators: A Foundation for High-Entropy Energy and Sensing Systems," *MRS Bulletin* 50 (2025): 258–270, https://doi.org/10.1557/s43577-024-00858-8.

Supporting Information

Additional supporting information can be found online in the Supporting Information section.

Supporting File 1: smll73728-sup-0001-SuppMat.docx.

Supporting File 2: smll73728-sup-0002-VideoS1.mp4.

Supporting File 3: smll73728-sup-0003-VideoS2.mp4.

16136829, 2026, 36, Downloaded from https://onlinelibrary.wiley.com/doi/10.1002/smll.73728 by Cas-Beijing Institution Of, Wiley Online Library on [29/06/2026]. See the Terms and Conditions (https://onlinelibrary.wiley.com/terms-and-conditions) on Wiley Online Library for rules of use; OA articles are governed by the applicable Creative Commons License